NASA-CR-205246

Comparison of modeled backscatter using measured aerosol microphysics with focused CW lidar data over Pacific

Vandana Srivastava
Global Hydrology and Climate Center, Universities Space Research Association, Huntsville, Alabama

Antony D. Clarke
Department of Oceanography, University of Hawaii, Honolulu

Maurice A. Jarzembski and Jeffry Rothermel
NASA Global Hydrology and Climate Center, Huntsville, Alabama

Abstract. During NASA's GLObal Backscatter Experiment (GLOBE) II flight mission over the Pacific Ocean in May-June 1990, extensive aerosol backscatter data sets from two continuous wave, focused CO_2 Doppler lidars and an aerosol microphysics data set from a laser optical particle counter (LOPC) were obtained. Changes in aerosol loading in various air masses with associated changes in chemical composition, from sulfuric acid and sulfates to dustlike crustal material, significantly affected aerosol backscatter, causing variation of about 3 to 4 orders of magnitude. Some of the significant backscatter features encountered in different air masses were the low backscatter in subtropical air with even lower values in the tropics near the Intertropical Convergence Zone (ITCZ), highly variable backscatter in the ITCZ, mid-tropospheric aerosol backscatter background mode, and high backscatter in an Asian dust plume off the Japanese coast. Differences in aerosol composition and backscatter for northern and southern hemisphere also were observed. Using the LOPC measurements of physical and chemical aerosol properties, we determined the complex refractive index from three different aerosol mixture models to calculate backscatter. These values provided a well-defined envelope of modeled backscatter for various atmospheric conditions, giving good agreement with the lidar data over a horizontal sampling of ~18,000 km in the mid-troposphere.

1. Introduction

Aerosols form a complex system with varying composition, size, number distribution, morphology, and shape. These parameters govern the aerosol scattering properties at a given electromagnetic radiation wavelength and in turn are affected by the meteorological conditions, altitude, and geographic location of the air mass. As an example of one of these parameters, aerosols can occur in various compositions [*Prospero et al.*, 1983; *Clarke and Porter*, 1991; *Clarke*, 1993] such as sulfuric acid, sulfates, nitrates, minerals, dustlike crustal material, and sea salt, which can exist in pure form, as composites, or in complex mixed phases [*Tang and Munkelwitz*, 1977; *Tang et al.*, 1978]. This variety leads to a wide range of complex refractive indices of aerosols, thereby affecting their scattering.

It is difficult to measure all aerosol parameters required to exactly predict the scattering, since most of them cannot be simultaneously determined by one instrument. A combination of instruments is generally required to determine various aspects of aerosol microphysics [*Willeke and Baron*, 1993].

In addition, some parameters that are very difficult to measure, such as shape or morphology, are usually approximated through the use of different aerosol models. However, these models may lead to different scattering results [*Srivastava*, 1988]. To ascertain a model's validity, scope, and limitations, model results need to be compared with direct scattering measurements. Further, such comparisons of modeled scattering using in situ aerosol microphysics data inputs can lead to better understanding of aerosol chemical properties and morphology of the complex aerosol systems and how they can affect their scattering.

With increasing use of lidar remote sensing of various atmospheric parameters, more detailed aerosol backscatter variability is being detected [*Post*, 1984; *Tratt and Menzies*, 1994; *Vaughan et al.*, 1995; *Rothermel et al.*, 1989, 1996a], enhancing the need to better model aerosol backscatter for various applications, e.g., winds [*Baker et al.*, 1995]. Airborne and ground-based, pulsed and continuous wave (CW) lidars provide large-scale remotely sensed aerosol backscatter data [*Rothermel et al.*, 1996a; *Menzies and Tratt*, 1994]. CW CO_2 lidars provide data with very high sensitivity and high spatial/temporal resolution even in clean conditions [*Srivastava et al.*, 1995], measuring backscatter as low as 3×10^{-11} m^{-1} sr^{-1} in aerosol loading of fractions of a microgram per cubic meter of air. On the other hand, advanced aerosol counters can provide both detailed aerosol size distribution

and compositional information on relatively short timescales [*Clarke*, 1991, 1993]. With the use of the in situ aerosol microphysics data, aerosol backscatter from different compositions can be appropriately modeled. These modeled aerosol backscatter results can be compared with direct, coregistered lidar backscatter measurements, providing verification of the modeling of atmospheric aerosol scattering. As the ambient atmospheric conditions change, aerosols can undergo chemical and physical changes, giving rise to complex mixtures, possibly requiring different models. Thus airborne measurements with aerosol counters and lidars provide detailed variations in aerosol microphysics and scattering, respectively, while their intercomparison can indicate variations in aerosol mixtures and the best models to use.

2. Measurements

To extend the understanding of atmospheric aerosol backscatter distribution, the National Aeronautics and Space Administration (NASA) sponsored a GLObal Backscatter Experiment (GLOBE) flight survey mission over the Pacific Ocean in 1989 and 1990 [*Bowdle et al.*, 1991]. GLOBE consisted of a complement of various instruments on NASA's DC-8 aircraft, measuring various atmospheric aerosol properties. Among the various instruments flown were two NASA CO_2 Doppler lidars measuring aerosol backscatter [*Rothermel et al.*, 1996b]. In addition, one of the aerosol counters flown was the University of Hawaii's preconditioned laser optical particle counter (LOPC) [*Clarke*, 1991, 1993], providing in situ measurements of microphysical and chemical properties of the aerosols. The measurements were identified by the universal time coordinated (UTC) code at the time of data storage.

2.1. Lidar Backscatter Data

Direct lidar backscatter measurements were obtained with NASA/MSFC's focused, CW, coherent, homodyne CO_2 Doppler lidars operating at 9.1 and 10.6 μm wavelengths. These lidars transmitted focused radiation at ~50 m away from the aircraft in front of the aircraft's left wing into the atmosphere and received Doppler-shifted backscattered signal from the aerosols in the lidar sample volume. The measured signal spectrum was converted to signal-to-noise ratio (SNR) data [*Rothermel et al.*, 1996b; *Vaughan et al.*, 1989]. Measured SNR was converted to aerosol backscatter, β (m^{-1} sr^{-1}), by using radiometric lidar calibrations [*Jarzembski et al.*, 1996]. Coherent detection and a large lidar sample volume of ~6 × 10^2 m^3 [*Cutten et al.*, 1996] allowed high sensitivity and detection of low signals for clean aerosol conditions, making it possible to acquire good quality high-resolution data with 5 s integration time (an aircraft speed of ~200 m s^{-1} implies spatial resolution of ~1 km). A larger lidar sample volume implies more particles sampled in the lidar beam, leading to smoother signal peak averaged over the backscattered return from all particles and allows a better estimation of SNR in low signal conditions. In clean mid-tropospheric conditions the 9.1 and 10.6 lidars detected aerosol β as low as 5 × 10^{-12} m^{-1} sr^{-1} and 2 × 10^{-11} m^{-1} sr^{-1}, respectively. However, near the detection threshold there is more variability in both lidar data sets due to the added uncertainty of extracting low signals out of noise. The uncertainty for moderate to high β is ~24%;

however, for low $\beta < 5 \times 10^{-10}$ m^{-1} sr^{-1} it is ~36%. Details of lidar instrumentation, calibration, and sensitivity study are given elsewhere [*Rothermel et al.*, 1996b; *Jarzembski et al.*, 1996].

2.2. LOPC Aerosol Microphysics Data

The LOPC system [*Clarke*, 1991] consists of a modified laser aerosol spectrometer (LAS-X, PMS, Boulder, Colorado) operating at 0.6328 μm wavelength with 256 size bins for particle diameters ranging from 0.15 to 7.0 μm. It has five selectable inlets heated to different temperatures such that some compositions, depending on their volatility, can evaporate while the residual composition's size distribution can be measured. The LOPC system has the unique capability of providing information on separate size distributions for some of the most important aerosol components: sulfuric acid, ammonium sulfate and bisulfates, and dustlike crustal material. These compositions are the ones most frequently encountered in mid-tropospheric aerosols, and their fractions can be inferred from the LOPC [*Clarke and Porter*, 1991; *Clarke*, 1993]. The LOPC was mounted on the right side of the DC-8 aircraft in front of the right wing. Detailed descriptions of the instrumentation and calibration are given elsewhere [*Clarke*, 1991; *Porter et al.*, 1992].

The LOPC's preheater system successively heats the aerosol sample, drawn in from the ambient atmospheric conditions, to 40°C, 150°C, and 320°C in channels Ch1, Ch2, and Ch3, respectively. Aerosols are heated to 40°C in Ch1, giving a nearly dry total aerosol size distribution at relative humidity (RH) of ~10% within the LOPC due to partial evaporation of water component. In Ch2, aerosols are heated to 150°C, where the volatile sulfuric acid (SA) component of aerosol evaporates. In Ch3 they are further heated to 320°C, where the ammonium sulfate (AMS) component and any bisulfates evaporate, leaving the residual nonvolatile, refractory, dustlike (DS) crustal component. Differentiation between AMS and bisulfates is not possible. Each channel gives the number of particles in the given size bin as dN/dD, which can be integrated to give the total number of particles N_o [particles/cm^3 of air] in that channel, indicative of the aerosol loading. To improve count statistics for low concentration of coarse aerosols and shorten accumulation times, a virtual impactor (VI) [*Clarke*, 1991] is used along with the LOPC in channels Ch4 and Ch5. The VI Ch4-measured aerosol size distribution heated only to 40°C gives total dry aerosol content, while VI Ch5 heated to 320°C gives the distribution of the residual refractory dustlike crustal component after both the SA and the AMS components have evaporated.

In general, the uncertainty of the LOPC data is roughly 10% to 20%. However, for clean conditions with fewer large-particle counts the uncertainty can be higher depending on the sample time. In these cases the sample time was usually made longer to minimize this uncertainty. LOPC size distributions and forward scattering spectrometer probe (FSSP) data have been compared, giving fairly good agreement [*Porter et al.*, 1992; *Cutten et al.*, 1996].

The information available from the LOPC channels was used to model aerosol β. However, for comparison of the lidar β and modeling using the LOPC data it is important to note certain key differences in the two data sets. LOPC data averaging, as it cycles through its five channels, can vary from approximately

1 to 3 min per channel, leading to about 5 to 15 min per observation, implying spatial resolution of ~60 to 180 km. During an LOPC observation there can be nearly 60 to 180 lidar data points exhibiting the fine-scale aerosol variation within the LOPC sample. Air mass changes occurring during an LOPC observation are averaged over the finer-scale variation shown by the higher-resolution lidar data. In cloudy air or near cloud boundaries the aerosol loading can change so rapidly such that modeling with the LOPC data (averaged over highly variable conditions) can have limitations due to both long sampling times and loss of water in heated channels, which cannot be easily accounted for at high RH (discussed in section 3.2). Furthermore, the LOPC sample volume of ~1.7 × 10^{-3} m^3 is several orders of magnitude smaller than the lidar sample volume of ~600 m^3. In clean conditions, where there are only few large aerosols, even with the inclusion of VI channels LOPC can underestimate their number concentration and the modeled aerosol optical properties. Lidar, with its higher sample volume, is less susceptible to lower large particle count statistics and can perform well as long as the signal is above its detection threshold.

3. LOPC Data Analyses

The aerosol microphysics data provided by the LOPC must be interpreted for the aerosol β modeling to be performed. The volume fraction, v, of each component in each size bin was estimated from the distributions measured in different channels. In addition, LOPC operates at aircraft cabin temperature, resulting in dry aerosol size distribution well above the ambient. Hence the aerosol diameter, D, provided by LOPC was corrected to ambient conditions to get the actual aerosol diameter, D_A, compensating for possible loss of water content in the heating process (discussed in section 3.2).

3.1. Volume Fractions of Various Aerosol Components

By using the information in each channel the various components can be differentiated, and their fraction can be estimated. Thus, for a given component the differential volume fraction, v_i (where i represents either SA, AMS, or DS), in each size bin can be determined from the difference of the distributions in the various channels. For channels Ch1, Ch2, and Ch3 these are given as

$$v_{SA}(D) = \left[\frac{\left(\frac{dN}{dD}\right)_{Ch1} - \left(\frac{dN}{dD}\right)_{Ch2}}{\left(\frac{dN}{dD}\right)_{Ch1}} \right] \quad (1)$$

$$v_{AMS}(D) = \left[\frac{\left(\frac{dN}{dD}\right)_{Ch2} - \left(\frac{dN}{dD}\right)_{Ch3}}{\left(\frac{dN}{dD}\right)_{Ch1}} \right] \quad (2)$$

$$v_{DS}(D) = \left[\frac{\left(\frac{dN}{dD}\right)_{Ch3}}{\left(\frac{dN}{dD}\right)_{Ch1}} \right] , \quad (3)$$

and for the VI channels they are given as

$$v_{SA+AMS}(D) = \left[\frac{\left(\frac{dN}{dD}\right)_{Ch4} - \left(\frac{dN}{dD}\right)_{Ch5}}{\left(\frac{dN}{dD}\right)_{Ch4}} \right] , \quad (4)$$

$$v_{DS}(D) = \left[\frac{\left(\frac{dN}{dD}\right)_{Ch5}}{\left(\frac{dN}{dD}\right)_{Ch4}} \right] , \quad (5)$$

where dN/dD represents number of particles per cubic centimeter of air in a given size bin. Each component's v_i can be either integrated over all bins to get total volume fraction, V_i', or converted to differential volume in each bin and then integrated to get the component's total volume, V_i.

Figure 1 shows some aerosol number distributions, dN as a function of dry particle diameter D, measured by LOPC in channels Ch1-Ch5. Channels Ch1-Ch3 are shown in Figures 1a and 1c, while VI channels Ch4 and Ch5 are shown in Figures 1b and 1d. The distribution measured in Ch1 (solid line) represents nearly dry total aerosol content at 40°C. When the aerosol is heated to 150°C in Ch2, SA content and any residual water volatilizes, giving a different number distribution (dashed line). In Ch3 the aerosol is further heated to 320°C, where the sulfate component evaporates, leaving a dustlike refractory component distribution (dotted line). The difference between the distribution at 40°C and at 150°C gives an estimate of the concentration of SA content in the aerosol (equation (1)). Similarly, the difference between distribution at 150°C and 320°C provides the AMS content of the aerosol (equation (2)). The residual nonvolatile DS-like crustal or refractory content of aerosol is given by the distribution obtained at 320°C (equation (3)). Inclusion of VI in channels Ch4 and Ch5 shows enhanced retrieval of large particle counts. Since the VI channels do not include a middle channel heated to 150°C, the difference between Ch4 and Ch5 gives the combined fraction of the SA and AMS component (equation (4)), while Ch5 gives again the DS component (equation (5)). Thus, to distinguish between SA and AMS from channels Ch4 and Ch5, the ratio of the fraction of SA to AMS from the difference of channels Ch1, Ch2, and Ch3 (equations (1), (2), and (3)) is used. This allows the use of more robust VI-included size distribution measurement in channels Ch4 and Ch5 with component information available from channels Ch1-Ch3.

The example of LOPC size distribution data shown in Figure 1 is from GLOBE II, flight 12, in transit from Darwin, Australia, to Tokyo, Japan, obtained at ~8 km altitude. (GLOBE flight track details are given by Cutten et al. [1996]). Figures 1a and 1b show low aerosol concentration in the relatively clean subtropical conditions encountered in the early part of the flight around ~10°N. Channels Ch1-Ch3 show mostly SA and some AMS component with little or no DS. Mostly SA and AMS were found in subtropical conditions with some fine DS fraction as possible residue of continental effect. Similarly, Figures 1c and 1d show size distributions in Ch1-Ch5 with higher aerosol loading due to an Asian dust plume event mixed with some anthropogenic aerosols near the Japanese coast in the last part of the flight. The difference between the channels again gives an estimate of the volume
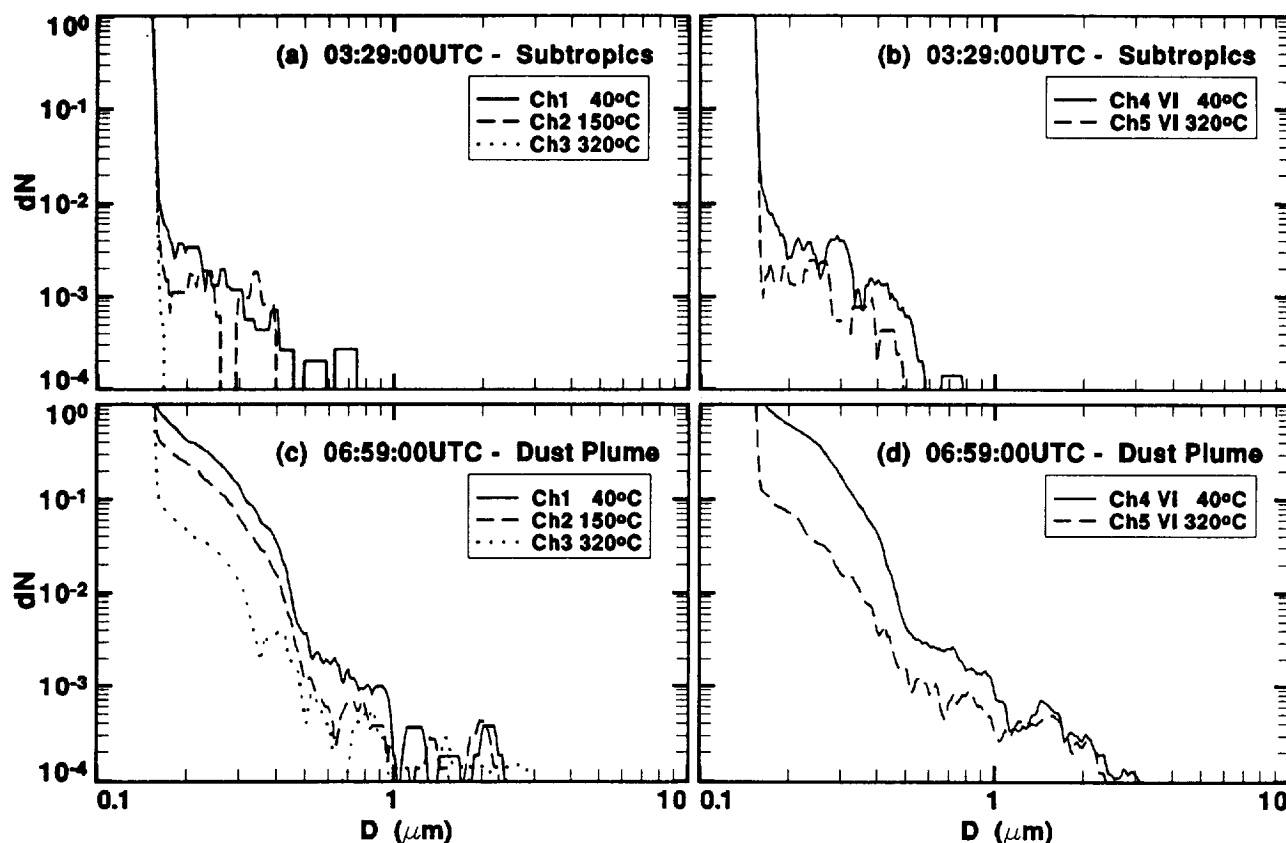
Figure 1. Aerosol size distribution data measured by LOPC in five heated channels, Ch1-Ch5. Two different data sets from GLOBE II flight F12, on May 31, 1990, from Darwin, Australia, to Tokyo, Japan, at ~8 km altitude show examples of: (a, b) clean tropical/subtropical aerosol loading at about ($7°N$, $134°W$), and (c, d) heavier aerosol loading at about ($34°N$, $139°W$) in an Asian dust plume.

fraction of various components of the sampled aerosols. In this case, larger particles were encountered with a significant amount of DS and some AMS and SA component. These figures demonstrate the changes in size distributions due to volatility of the aerosol components in different channels at given temperatures, as well as changes in the aerosol components under different atmospheric conditions.

3.2. Correction to Ambient Aerosol Size

Because of the large temperature increase in bringing free tropospheric ambient aerosols into the aircraft the RH drops significantly, causing the aerosols to lose most of their water content. Therefore the size obtained is nearly a dry diameter, D, measurement at the LOPC channel temperature and RH rather than at the ambient temperature and RH. The actual aerosol diameter, D_A, has to be determined at ambient atmospheric conditions outside the aircraft. Hence measured D was corrected for ambient aerosol water content to get D_A, which was used for modeling β. The procedure for extrapolating to D_A was done in postprocessing of the data by determining the growth of the aerosols from LOPC RH back to ambient RH, both of which were recorded as part of the data set. A growth factor, G, was applied to the measured distribution to get the consequent aerosol size change, resulting in a near-ambient aerosol size distribution.

Different aerosol compositions grow differently on the basis of their hygroscopicity. For example, SA, being very

hygroscopic, changes size dramatically as RH is changed, whereas DS-like crustal material hardly grows at low RH (for example, in the middle and upper troposphere). Growth for each component, i, of the aerosol can be given in terms of a growth factor $G_i=(D_A/D)_i$, where D and D_A are the dry and ambient diameter, respectively. Growth curves given by *Tang and Munkelwitz* [1977] and *Tang et al.* [1978] for SA and AMS were used for estimating growth factors G_{SA} and G_{AMS}. However, growth for DS, G_{DS}, can be very complex [*Hanel*, 1976; *Hanel and Lehmann*, 1981], depending on its mineral content and possible sulfate coatings; hence for simplicity an average activity factor of ~0.1 has been assumed to get G_{DS}. Growth is primarily dominated by the SA component, as it is significantly more hygroscopic than AMS or DS. Once the volume fractions of the components have been estimated by using equations (1)-(5), G_i can be determined for each bin size.

The method of estimating aerosol growth also depends on the type of aerosol mixture. In the simple case in which each aerosol is made of a pure single component with no mixing, D_A for the individual aerosol component for the each size bin can be estimated by multiplying D_i by its respective G_i. In cases in which aerosols can have two or more mixed components, growth would depend on their v_i in the mixture; therefore a volume-weighted approach was used. The effective volume-weighted growth, G_e, for mixed aerosols can be obtained from the component's G_i on the basis of its v_i in each size bin as

$$G_e = \left\{ \Sigma(G_i)^3 * v_i \right\}^{1/3}, \qquad (6)$$

where the summation over i stands for the components present in mixed aerosol. In the case of $v_i = 1$, (6) reduces to $G_e = G_i$, going back to the single-component growth. The ambient mixed aerosol diameter is given by $D_A = G_e * D$. The G_e changes slightly for each size bin, as the composition fractions can change in different size bins, as seen in Figure 1. For a complex aerosol system in which composition can vary for different sizes this size dependent growth provides a simple but more realistic estimation of D_A in comparison with assuming a single growth factor for the entire distribution. In addition, it allows for two or more components to be mixed, depending on different aerosol models.

The growth factor was further used to estimate the volume fraction of the water content lost on heating the aerosols in the LOPC channels in each size bin. The volume fraction of water for each component, $v_{W,i}$, can be given in terms of the growth factor G_i for the pure aerosol case as

$$v_{W,i[e]} = 1 - \frac{1}{G_{i[e]}^3}, \qquad (7)$$

where for the mixed aerosol case the subscript i is replaced by e, using G_e for mixed components. The water volume fraction contribution to backscatter can be taken into account by using v_W estimates.

Even though G_{SA} dominated the aerosol growth, a volume-weighted growth approximation was adopted for mixed aerosols to account for any AMS and DS effect and for consistency as a similar approach was employed in the commonly used volume-weighted effective refractive index discussed next. Both the G_i and the G_e may be limited for very high RH (beyond the deliquescent point of solids) but are fairly adequate for size changes for β applications in the range of RH of 5% to 60% in the middle and upper troposphere encountered during GLOBE.

4. Aerosol Backscatter Modeling

Atmospheric aerosol backscatter, β, at a given radiation wavelength, λ, depends on D_A and composition characterized by the complex refractive index, m. For different v_i, m can be estimated from LOPC data (equations (1)-(5)). Various aerosol mixing models can be used, since atmospheric aerosols are continuously changing and interacting as the ambient conditions are changing, giving rise to complex structures. Consequently, aerosol compositions can occur in a variety of configurations or mixtures. It is almost impossible to predict exactly how these compositions are mixed in an atmospheric aerosol ensemble; however, some plausible models can be formulated for certain conditions to simulate them. In very clean conditions frequently encountered in remote marine atmosphere, newly produced aerosols may exist separately as pure components for short periods of time (a few minutes to a few hours). As these aerosols age and mix in changing air masses, they tend to lose their pure and simple configuration, becoming partially mixed because of growth by diffusion, deposition, coagulation, or cloud processes. They may be more stable and have longer lifetimes (of the order several hours to days). In marine mid-troposphere these may be predominantly acidic sulfates with possibly some fine dust com-

ponent residual of continental effect, or on a few occasions they may contain some large sea-salt particles in very strong convective updrafts. The dust component may or may not become composited with sulfuric acid and sulfates. In aged continental air masses there can be significant increase in dust or pollution-type aerosols. These can have varying lifetimes (a few hours to days or even weeks) and can be advected over considerably long distances, thus giving rise to a high probability of completely mixing with acids and sulfates in internally mixed composites or even coated particles.

To deal with these different scenarios, three simple aerosol models were chosen to calculate m and β to assess the effect of different mixing: (a) pure, (b) partially mixed, and (c) completely mixed components. These three models provide a fairly good range of possibilities for various intermediate cases that may exist. Figure 2 shows a simplified schematic of the three models with random volumes of different components. In the mixed cases the volume fractions are represented as pie fractions, which would, however, be randomly dispersed within the particle [Srivastava, 1988]. Another specific model deals with an intermediate case of coated particles that may exist in the atmosphere. This model is more difficult to evaluate, since it is hard to accurately determine the coating thickness or its chemical properties if the coating is a complex mixture. Thus it would require additional assumptions on the size and kind of thickness;
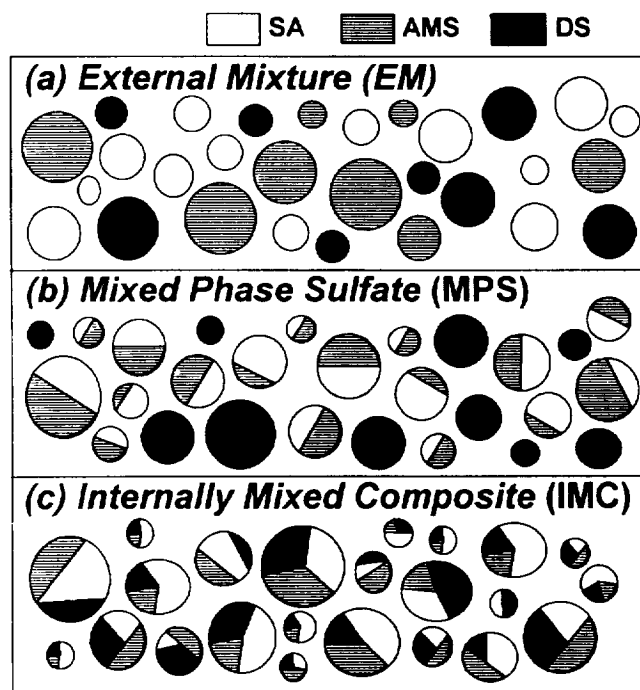

Figure 2. Schematic of three different aerosol models: (a) external mixture (EM), in which all components, SA, AMS, and DS are separate, (b) mixed-phase sulfate (MPS), in which only SA and AMS are randomly mixed together with varying volume fractions while DS is separate, and (c) internally mixed composite (IMC), in which SA, AMS, and DS are randomly mixed together within each particle in varying volume fractions. For simplicity in mixed particles the volumes are schematically shown as pie fractions, which, however, would be randomly distributed within the particle.

hence for simplicity, only a general internally mixed composite model is treated here in case (c).

Aerosol backscatter modeling was performed by using Mie theory [Mie, 1908], assuming a spherical shape for the aerosols. This fits well for SA and also can be applied satisfactorily for AMS, which, being hygroscopic, may generally be slightly wet amorphous structures resembling rough spheres. The DS component, however, would be nonspherical, and for these cases, Mie theory is an approximation. However, for long wavelengths this assumption has given reasonable results [Cutten et al., 1996]. For shorter wavelengths, nonsphericity may become significant. Complex refractive indices of pure SA, AMS, and DS aerosols [Srivastava et al., 1992, 1995; Kent et al., 1983] and water at the two CO_2 lidar wavelengths were obtained from refractive index measurements [Shettle and Fenn, 1979; Toon et al., 1976; Palmer and Williams, 1975; Hale and Querry, 1973].

4.1. External Mixture Model

In the simple external mixture (EM) aerosol model, SA, AMS, and DS are assumed to be separate pure components (Figure 2a). This situation may be expected to occur in clean mid-troposphere, especially in the tropical regions, where new particle formation is more likely [Clarke, 1993], giving less chance for intermixing. In this model therefore the effective complex refractive index, m_{i+W}, of each aerosol is calculated from its pure component fraction along with water fraction as estimated by the growth (equations (6) and (7)). Thus m_{i+W} of ambient aerosols can be given by the volume-weighted average of each m_i with v_i and m_W with $v_{W,i}$ as

$$m_{SA+W} = v_{SA} m_{SA} + v_{W,SA} m_W \tag{8a}$$

$$m_{AMS+W} = v_{AMS} m_{AMS} + v_{W,AMS} m_W \tag{8b}$$

$$m_{DS+W} = v_{DS} m_{DS} + v_{W,DS} m_W . \tag{8c}$$

The water content associated with the AMS and DS component was almost negligible for the low mid-tropospheric RH. The most significant effect of water is felt by the hygroscopic SA component; however, the growth in the radii is slightly offset by the dilution effect of water to m_{SA+W}. With m_{i+W} estimation at a given wavelength (equations (8a-8c)), the single-particle backscatter cross section, $\sigma_i(D_A, m_{i+W}, \lambda)$ (m^2 sr^{-1}) is calculated using Mie theory. For the EM model the total backscatter coefficient, β is given by

$$\beta = \int \sigma_{SA}\left(D_A, m_{SA+W}, \lambda\right)\left[\frac{dN}{dD_A}\right]_{SA} dD_A$$

$$+ \int \sigma_{AMS}\left(D_A, m_{AMS+W}, \lambda\right)\left[\frac{dN}{dD_A}\right]_{AMS} dD_A$$

$$+ \int \sigma_{DS}\left(D_A, m_{DS+W}, \lambda\right)\left[\frac{dN}{dD_A}\right]_{DS} dD_A \tag{9}$$

where $[dN/dD_A]_{SA \text{ or } AMS \text{ or } DS}$ is obtained from channels Ch1-Ch5 given by equations (1)-(5).

4.2. Mixed-Phase Sulfate Model

In the mixed-phase sulfate (MPS) model, SA and AMS are mixed internally in one particle and DS component remains

separate (Figure 2b). These may occur in slightly older, partially mixed air masses where the probability of mixed-phase ammoniated sulfates is high though the DS component may not have had a chance to get mixed in. These can chemically react and form bisulfates or other intermediate sulfates. However, the optical scattering properties of bisulfates are not well known in the infrared. Hence a volume-weighted physical mixture of the individual SA and AMS properties has been assumed as internally mixed, while DS is treated separately as an external component. In this case the effective complex refractive index of mixed sulfate, m_{MPS}, is calculated for each size bin by using complex refractive indices of SA, AMS, and water along with their v_i as

$$m_{MPS} = v_{SA} m_{SA} + v_{AMS} m_{AMS} + v_{W,MPS} m_W, \tag{10a}$$

and for DS as given before by

$$m_{DS+W} = v_{DS} m_{DS} + v_{W,DS} m_W, \tag{10b}$$

where the $v_{W,MPS}$ is the water volume fraction in the MPS component (equation (7), with $G_e \equiv G_{MPS}$) and $v_{W,DS}$ is in the unmixed DS component. Volume fractions of the components are obtained from the difference of the LOPC Ch1 to Ch3 as given in equations (1)-(3). As we noted above, $\sigma_{MPS}\left(D_A, m_{MPS}, \lambda\right)$ for the mixed sulfate is calculated with the mixed sulfate effective complex refractive index and for the DS component separately. For the MPS model the total backscatter, β, is obtained by

$$\beta = \int \sigma_{MPS}\left(D_A, m_{MPS}, \lambda\right)\left[\frac{dN}{dD_A}\right]_{SA+AMS} dD_A$$

$$+ \int \sigma_{DS}\left(D_A, m_{DS+W}, \lambda\right)\left[\frac{dN}{dD_A}\right]_{DS} dD_A, \tag{11}$$

where $[dN/dD_A]_{SA+AMS}$ is obtained from equation (4) as the difference between Ch4 and Ch5.

4.3. Internally Mixed Composite Model

This internally mixed composite (IMC) model contains SA, AMS, and DS mixed in one composite aerosol (Figure 2c). This type of aerosol may occur in fairly aged complex air masses, such as pollution or continental dust plumes, that may be advected for long distances before dissipating like the Asiatic dust plume over the Pacific Ocean encountered off the coast of Japan. This would also be suited for complex boundary layer aerosols, high-humidity regions, and cloud-pumped aerosols. The effective complex refractive index, m_{IMC}, of the composite aerosol is obtained by volume averaging of m_i and m_W as

$$m_{IMC} = v_{SA} m_{SA} + v_{AM} m_{AM} + v_{DS} m_{DS} + v_{W,IMC} m_W, \tag{12}$$

where $v_{W,IMC}$ is water volume fraction in the composite aerosol (equation (7), with $G_e \equiv G_{IMC}$). In the IMC model, $\sigma_{IMC}(D_A, m_{IMC}, \lambda)$ for the composite aerosol is calculated with m_{IMC} to give total β as

$$\beta = \int \sigma_{IMC}\left(D_A, m_{IMC}, \lambda\right)\left[\frac{dN}{dD_A}\right]_{SA+AMS+DS} dD_A, \tag{13}$$

where $[dN/dD_A]_{SA+AMS+DS}$ is for total aerosol distribution obtained from Ch4.

5. Comparison of β Modeling With Lidar Data

Results of backscatter, $\beta(9.1)$, calculations for the EM model (equation (9)), the MPS model (equation (11)), and the IMC model (equation (13)) using the LOPC data were compared with direct β measured by the 9.1 μm CW lidar. For a given LOPC datum, β calculations using the three models are associated with the same experimental uncertainty; however, the difference in the β values shows the uncertainty involved with the way in which the aerosol composition is modeled. Thus the three models give a good envelope of the effect of changing the mixture models for estimating the complex refractive index and hence the scattering properties for inhomogeneous aerosols. Where the three models predict close values, the choice of the mixture model is not as significant; however, when the values differ, the model that best agrees with the lidar data would represent the best model for the aerosols. In addition, for a given air mass containing several LOPC data points, one particular model may overlap more with the lidar data than the other two models and thus can be considered as the best representation of the aerosol model for such an air mass. Therefore, even though the aerosol β varies over ~6 orders of magnitude and all three models track the lidar data fairly well, a time series comparison of LOPC modeled β with the lidar β gives an approximate indication of which model may be preferred for different air masses encountered during the GLOBE flights.

LOPC data and lidar measurements, in section 5.1, are chosen from representative GLOBE flights over the Pacific Ocean with 6 to 8 hour periods at almost constant cruising altitude of about 8.0 to 8.5 km. Details of the GLOBE II flight tracks, with latitude and longitude, are given in Figure 1 of *Cutten et al.* [1996]. Four flights (F6, F10, F12, F14) shown here gave some very significant marine mid-tropospheric features and good horizontal sampling of changes in aerosol chemical and physical properties in large air masses over synoptic scales. Also, these showed some differences in the northern and southern hemispheric aerosol systems. In section 5.2, histograms of the aerosol β distribution are shown for both modeled and measured β. Section 5.3 compares LOPC data with the 10.6 μm CW lidar data along with the ratio of $\beta(9.1)$ to $\beta(10.6)$ from both the lidar data sets and the LOPC modeling.

5.1. Flight Data

Figures for each of the flights show temporal variation of several parameters: (1) ambient RH data obtained by the DC-8 aircraft instrumentation data sets, (2) total aerosol number density, No, integrated from LOPC Ch4 size distribution, (3) aerosol composition for SA, AMS, and DS in terms of the total integrated volumes, V_{SA}, V_{AMS}, and V_{DS}, obtained from equations (1)-(5) for each sampled distribution during the flight, (4) modeled $\beta(9.1)$ results using the EM, MPS, and IMC models (equations (8)-(13)), and (5) calibrated CW lidar β (9.1) data.

5.1.1 Hawaii to Samoa F6. This flight was deployed on May 20-21, 1990, from Honolulu, Hawaii, to Pago Pago, American Samoa, giving a crossover sampling from northern to southern hemisphere, encountering the ITCZ (Figure 3). Good qualitative agreement was obtained between the CW lidar β and calculated β from the three models, showing similar temporal variation. A similar trend was also seen in the micro-
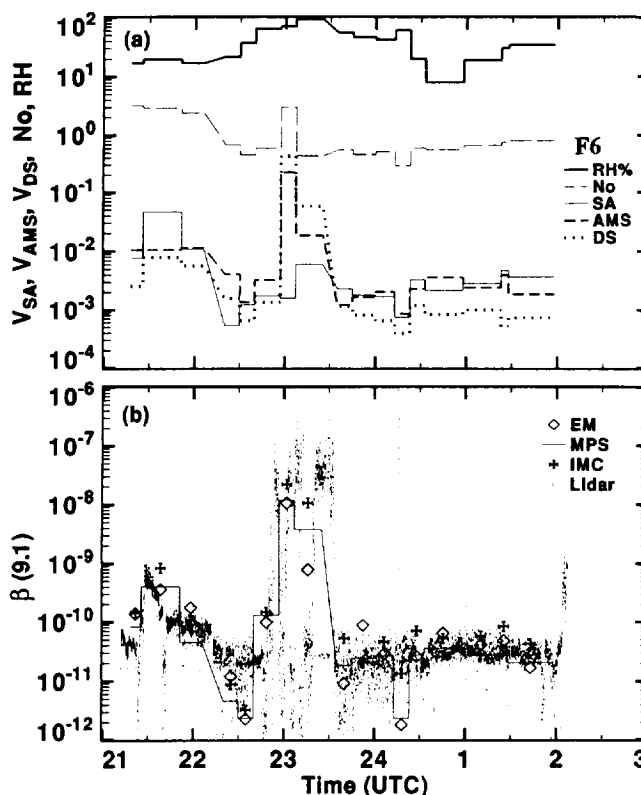

Figure 3. Time series of F6 data from Honolulu, Hawaii, to Pago Pago, American Samoa, on May 20-21, 1990: (a) atmospheric relative humidity (RH), total aerosol concentration (No, number of particles per cubic centimeters of air), and total volumes of each component (V_{SA}, V_{AMS}, and V_{DS}, $\mu m^3/m^3$ of air) obtained from LOPC size distributions using equations (1)-(5) and integrated over all size bins; and (b) comparison of the $\beta(9.1)$ lidar data with the EM, MPS, and IMC models using equations (8)-(13). MPS model results are given as solid line showing the time duration of each LOPC sample, whereas EM and IMC are shown as diamonds and crosses, respectively, at the midpoint of the sample time to minimize data overlap.

physical LOPC total No data and component volume fractions; however, relative volumes of each component changed during the flight, affecting β. Initially, there was more V_{SA} content, suggesting Hawaiian volcanic influence and possible dimethyl sulfide (DMS)-derived SA mixed in with a frontal development that was taking place near the island. This led to slightly elevated β that dropped further away from the island and approaching the tropical region. Around 2245 UTC the ITCZ was encountered with high RH, strong convective updrafts, variable cloud cover, and variable β. The side-viewing video record on board the DC-8 showed that the aircraft was flying mostly in a cloud-free low to moderate β region between high-level cirrus clouds and low-level cumulus/altocumulus clouds. However, occasionally, the convection would be so deep that the altocumulus and the cirrus would thicken and merge completely associated with significant increase in β. Strong updrafts were seen in the concurrent European Commonwealth Meteorological Weather Forecasting (ECMWF) data (E. W. McCaul Jr., private communication, 1994). The convectively
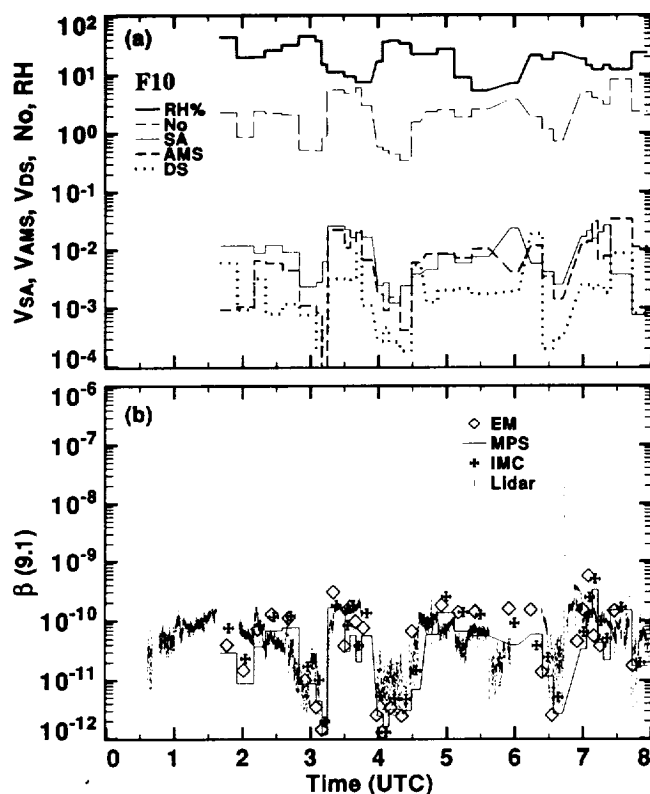
Figure 4. Same as Figure 3 for data from F10 from Christchurch, New Zealand, to Melbourne, Australia, on May 28, 1990.

active regions in the ITCZ lifted the high-RH marine boundary layer (MBL) air, possibly detraining it into the cloud-free regions between the cirrus and the altocumulus through cloud-pumping processes. Interestingly, along with enhanced total N_o, the composition of the particles (aerosol or cloud) also showed this effect, giving a higher fraction of nonvolatile component in the heated channels Ch3 and Ch5. Usually in mid-troposphere, Ch3 and Ch5 reflect the nonvolatile DS component, but in this case there was no nearby source of DS. Furthermore, strong upward motion registered in ECMWF data suggest that this large size nonvolatile aerosol content would most likely be nonvolatile sea-salt particles carried upward from the MBL through convective cloud-pumping processes up to the ~8 km flight altitude. Assumption of DS versus sea salt in the ITCZ only gives ~26% variation, as the DS to sea-salt refractive index change is offset by the hygroscopicity change registered in size and high water content, lessening the total effect on β. Choosing sea salt in the IMC model for Ch3 or Ch5 in the ITCZ would give $\beta \sim 2.97 \times 10^{-8}$ m^{-1} sr^{-1} at 2307 UTC and $\beta \sim 7.96 \times 10^{-9}$m^{-1} sr^{-1} at 2325 UTC as in comparison with DS (shown in Figure 3), which gave $\beta \sim 2.22 \times 10^{-8}$ m^{-1} sr^{-1} and 1.07×10^{-8} m^{-1} sr^{-1}, respectively. Even so, the change in β in the ITCZ was both measured by the lidar and predicted by the models. Furthermore, these aerosols also contained more AMS component than SA. Outside the ITCZ region after 2330 UTC, subsidence brought stable cleaner air, lowering β to very clean tropical air values, sometimes even below the detection thresholds. In the southern hemisphere a stable clean air mass was encountered almost to Samoa with comparable SA and AMS content, giving uniformly low β values. Lidar β and LOPC N_o showed a similar trend, giving

positive correlation showing the consistency between the two data sets, as these quantities are directly proportional to each other. Also, there was occasional positive correlation between RH and N_o and between RH and β, for example, in the ITCZ, while at other times, for example, in tropical air masses, they were poorly correlated, as there is no straightforward relationship between the two parameters.

In this flight, three distinct air masses were sampled: the subtropical air mass near Hawaii with some superimposed island land mass effect, an extremely convective air mass in the ITCZ's with variable backscatter, and then a clean, more stable, tropical air mass all the way to Samoa. All three models agree reasonably well with the lidar β, providing a good envelope of modeled β for different possible scenarios of mixing aerosol components. Within the envelope the overall experimental uncertainty (LOPC size measurement errors, growth errors, and refractive index errors) is common to all three models; hence these models can be intercompared to see which one may be preferred for a given air mass. For tropical and subtropical air mass in F6 the MPS model overall was in closest agreement with the lidar β, but IMC and EM were not very far off. This finding suggests that in the tropics and subtropics a fairly simple aerosol system was encountered with possible partial mixing of SA and AMS. Since there wasn't much DS in these areas, it does not matter whether or not one chooses a composite mixture. Agreement of the EM model with lidar β implies that the simple pure model works well for newly formed aerosols existing in clean and fresh conditions. Occasionally, when aerosol loading was very low accompanied by low β values, the LOPC modeled β was even lower than lidar β, with the three models giving quite different results. This discrepancy was caused by the LOPC's inability to sample effectively the more dispersed fewer large particles that provide major contribution to β as compared to the lidar, which has larger sample volume and fewer count statistics problems. In addition, this sampling inefficiency in the larger size bins can slightly bias one channel with respect to others, adding uncertainty in the estimation of large-particle composition and v_i and thereby leading to deviations in β results from the three models.

5.1.2 New Zealand to Australia F10.

A comparison similar to that for F6 was performed for F10, deployed on May 28, 1990, from Christchurch, New Zealand, to Melbourne, Australia (Figure 4). This flight showed relatively low aerosol counts and low $\beta \sim 10^{-10}$ m^{-1} sr^{-1} in the southern hemispheric late fall clean conditions. However, there is less fine-scale variation than can be seen in F6 and more larger-scale variability, suggesting that change in air masses was encountered during this long transit flight. There is also more variability in N_o and the component fractions. Overall, the large-particle concentration was low; however, the small-particle concentration was considerable, giving moderate N_o values, which allowed reasonable differentiation of the component fractions. In comparison the DS component was quite low almost throughout this flight, showing less land mass influence in the southern hemisphere over the Pacific as expected. Interestingly, these small-size particles were mostly dominated by the SA component in southern hemisphere mid-tropospheric aerosols. This domination suggests a possible stratospheric/ tropospheric exchange, leading to higher SA from volcanic origin, probably from the eruption of Kelut in February 1990, which dumped small-sized SA aerosols in the stratosphere, in agreement with the observations of *Kent et al.*, [1995]; however, fresh SA may also occur from gas-to-particle conversion
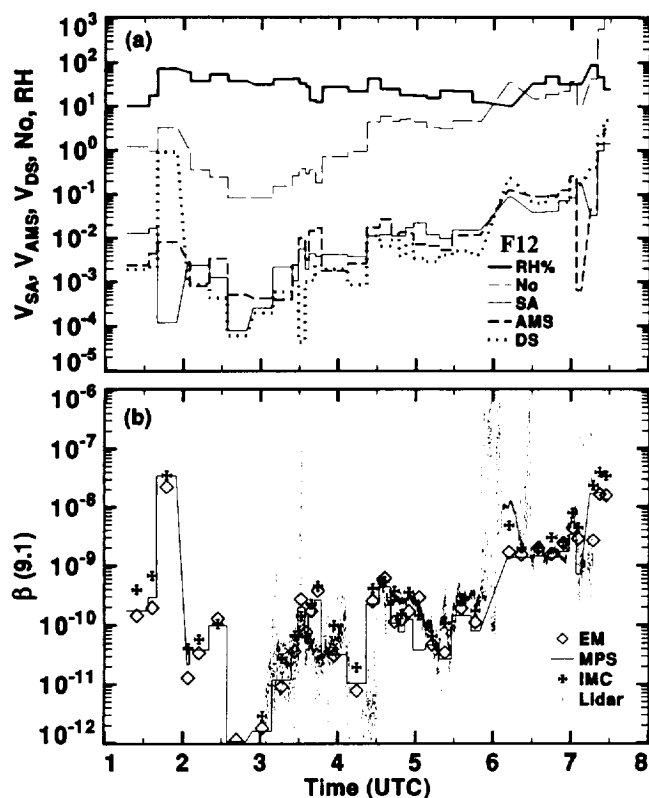
Figure 5. Same as Figure 3 for F12 data from Darwin, Australia, to Tokyo, Japan, on May 31, 1990.

[*Clarke*, 1993]. Two cases of tropospheric/stratospheric exchange were seen in ECMWF data (E. W. McCaul Jr., private communication, 1994) just after 0300 UTC and around 0630 UTC with lowering of the tropopause and possible entrainment of stratospheric air, making both No and β dip low. RH data were mostly anticorrelated with No, V_{SA}, and β. V_{SA} and V_{AMS} nearly follow each other, suggesting that the entire air mass sampled was of similar composition with low V_{DS}, except for regions of stratospheric SA intrusion. In general, the southern hemispheric No was lower than the northern hemispheric aerosol loading but was still slightly higher than the clean tropical air masses encountered in F6.

As in F6, the three aerosol mixture models show the same trends in β as those seen in the lidar data. Any of the three models could possibly be chosen for such an air mass; however, occasionally, there is deviation between the lidar β and the modeled β. Even though the air was fairly clean with low β, the EM model (generally applicable for clean fresh aerosol system) seems to depart more from the lidar data than it did for F6, while the MPS and IMC models give more overlap. This finding suggests that possibly the aerosol system may not be as relatively fresh as in the tropics, being more aged with fine mode residual of either volcanic or continental origin with more complex mixture.

5.1.3 Australia to Japan F12 On May 31, 1990, F12 crossed over from southern to northern hemisphere, again flying through the ITCZ in a different tropical region from Darwin, Australia, to Tokyo, Japan, where an Asiatic dust plume was encountered. Figure 5 shows the comparison for F12. Initially clean subtropical conditions followed by the ITCZ (around 0200 UTC) were encountered in the southern hemisphere. In the ITCZ, LOPC data measured broad size dis-

tributions in all channels, suggesting large-size nonvolatile sea-salt aerosols yielding high β as in a similar feature observed in F6, associated with strong convective pumping carrying large-size MBL particles at the aircraft altitude. In the very clean tropical region near the equator (crossed around ~0235 UTC) the aerosol loading and β dropped to threshold levels of both instruments. In addition, very high fine-particle counts were reported with a condensation nuclei (CN) counter on board the aircraft [*Clarke*, 1993], showing a region of significant new particle production that was mostly pure SA. Further on, the aerosol concentration steadily increased in the northern hemisphere to the levels of marine subtropical air mass until 0430 UTC. Even though β conditions were low, there was a lot of variation in comparison with the more stable subtropical air mass in F6. After 0430 UTC there was a distinct change in the air mass with higher No and more SA, AMS, and DS component (Figure 5a) with the encountering of the Asian continental landmass effect with moderate β values. Around 0600 UTC, DS increased significantly along with β.

Till ~0430 UTC for subtropical air mass, most of the aerosol models show fair agreement, though the overall best fit is given by the MPS model. After ~0430 UTC, when the Asian continental aerosol was encountered with more AMS and DS, the IMC model gave closer overlap. This aerosol system was aged, probably well mixed, though diluted by clean marine tropospheric air until ~0600 UTC. Afterward the air mass showed pronounced continental effect at the flight level. In the continental DS plume, with or without marine air dilution, the aerosol was most likely an internally mixed composite; hence the IMC model led to the closest agreement with lidar β.

5.1.4 Japan to Hawaii F14. A transit flight F14 was deployed on June 3-4, 1990, from Tokyo, Japan, to Honolulu, Hawaii, giving a good sampling of northern hemispheric remote regions with the effect of transport of large continental air mass over the ocean. Figure 6 shows the data comparison. Initially, extremely high β due to Tokyo pollution was encountered superimposed on the Asian dust plume event in a high-RH environment. After 2400 UTC, the air mass changed with high DS and AMS content. Around 0200 UTC, some high-RH air mass was encountered for a short period representing cloudy air. In this case, high lidar β was encountered, and the modeled β showed similar increase but was somewhat lower, probably because of underestimation of D_A of large wet aerosols and cloud particles in very high RH. After the brief high RH period, however, drier air mass than before was encountered. Changes in β in this air mass showed variations in the continental plume due to mixing and consequent dilution with clean marine tropospheric air. Nearer Hawaii at ~0345 UTC the air mass abruptly changed with β decreasing by about 2 orders of magnitude to very clean subtropical mid-tropospheric levels with almost no continental effect. Lidar β was low, close to its detection threshold. The particle counts also showed a dramatic drop-off, with lower RH and composition changed to primarily SA with only occasional AMS and negligible trace DS. Finally, during landing in Hawaii, higher β was encountered for a short period due to some local AMS and DS source.

For high aerosol loading till ~0400 UTC, all three models gave β close to lidar data; however, the IMC model gave the best overlap with lidar β, again suggesting that the aerosols were aged well-mixed composites that have been advected over the clean marine mid-troposphere. For clean subtropical case the MPS model gave the best agreement with lidar data, while the IMC model, which is better suited for aged well-mixed
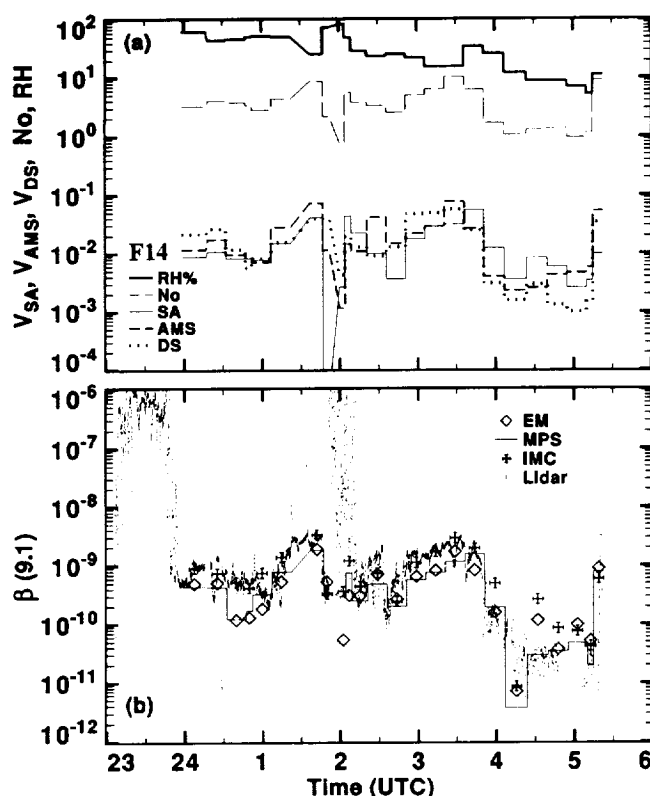
**Figure 6.** Same as Figure 3 for F14 data from Tokyo, Japan, to Honolulu, Hawaii, on June 3-4, 1990.

Figure 7. Comparison of the histograms of measured $\beta(9.1)$ from CW lidar and modeled $\beta(9.1)$ using the LOPC data for F6, F10, F12, and F14 (shown in Figures 3, 4, 5, and 6).

aerosols, did not agree as well. This finding suggests that the clean subtropical aerosol system is primarily composed of small-size SA aerosols with partial ammoniation as shown by the measured LOPC V_i. There was some variation in the LOPC data, and different models showed higher uncertainty during very clean conditions due to the inefficiency of large-particle sampling as discussed earlier. During landing, all three models gave similar β results, well within the rapidly changing lidar β.

The flights shown here sampled different mid-tropospheric regions and conditions during GLOBE. For some GLOBE flights the preferred models predicted for a given air mass have been used with the LOPC data and compared with the FSSP data calculations of β, giving good agreement [*Cutten et al.*,1996].

5.2. Aerosol Backscatter Distribution

The frequency of occurrence of $\beta(9.1)$ in Figure 7 shows the marine mid-tropospheric aerosol backscatter distribution sampled during the four flights. Data in Figure 7a show the mode of $\beta \sim 3.5 \times 10^{-11}$ m^{-1} sr^{-1}, which agrees with the mode in Figure 6b of *Cutten et al.* [1996] (both of these figures are subsets of the overall GLOBE flight statistics shown in Figure 2 of *Rothermel et al.* [1996a]). Figure 7a has much better smooth statistics with about 100 times more lidar data points than the 109 LOPC data points shown in Figures 7b, 7c, 7d for the three aerosol models. The LOPC data gave relatively more extremely low β occurrences, because in very clean atmospheric conditions it could not effectively sample the few large particles that would tend to increase the total β, whereas the lidar with its large sample volume could detect them well and consequently was not biased toward very low β. In spite of the
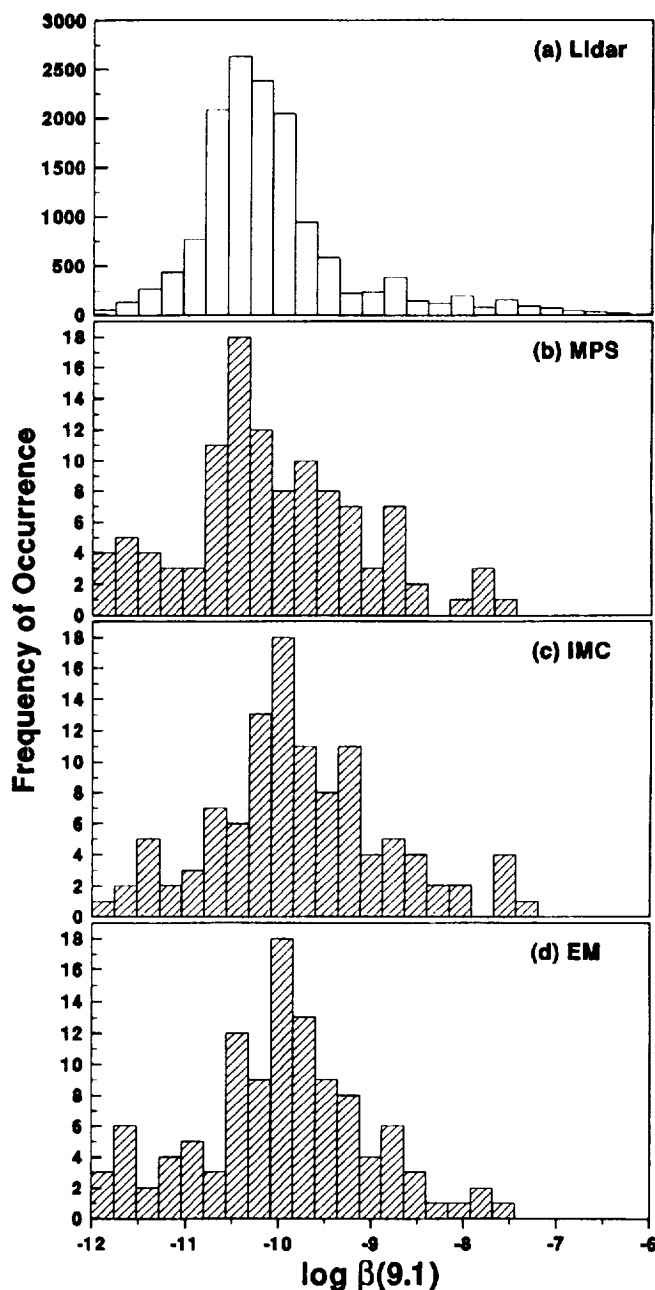
overwhelming difference in data resolution and the sampling volumes between the lidar and the LOPC, all three β models show the presence of the mid-tropospheric background aerosol [*Rothermel et al.*, 1989, 1996a; *Cutten et al.*, 1996; *Pueschel et al.*, 1994] similar to the lidar β. However, the MPS model (Figure 7b) gave very good agreement with the lidar β, both showing the background mode ~3.5 × 10^{-11} m^{-1} sr^{-1}. The IMC and EM models were slightly offset in the mode value, predicting it at ~1 × 10^{-10} m^{-1} sr^{-1}.

The use of the MPS model represents the first time that the measured aerosol microphysics has been able to predict the value of the aerosol background β mode in such good agreement with lidar β. This ability also reflects the possible compositional mixture of the background aerosol itself [*Srivastava et al.*, 1995], suggesting that the background

aerosol is primarily SA with some AMS that has had sufficient time for the sulfates to have been mixed with each other, but the trace DS component is generally unmixed. The background mode seems due neither entirely to a very fresh aerosol system nor to a very aged one. If it is primarily the freshest short-lived pure SA, then the EM model would tend to agree; if it is a well-mixed, very aged coarse aerosol, then the IMC model would agree. Instead it seems to be a residual aerosol system emerging from an equilibrium between the sources (that produce fresh aerosols into it) and the sinks (that remove aged, well-mixed aerosols from it). Thus this quasi-stable background aerosol may predominantly consist of partially mixed SA and AMS, in an MPS mixture, with trace DS.

All three models also showed another higher-β mode at ~1.7 × 10^{-9}m^{-1} sr^{-1}, comparing well with the lidar β. This type of analysis shows that different mixture models not only give different results for a single data point but also could give slightly different statistical results. Comparison with direct lidar data gives some indication of the chemical structure of the dominant aerosol mode in the MPS model.

5.3. Backscatter Ratio for 9.1 and 10.6 μm

The other CW lidar measured β at 10.6 μm, which gave a two-wavelength β comparison, leading to some aerosol composition diagnosis [Srivastava et al., 1995]. For most of F6 and F10, β(10.6) was below the lidar's sensitivity level. Figure 8a shows comparison of modeled β(10.6) from LOPC data with lidar β(10.6) for F12 and F14 compiled together. There was very good agreement between the IMC model and lidar β for the aged continental plume over the Pacific, whereas for the fresh small-size aerosols in clean conditions the MPS model was in better agreement. This agreement reconfirmed the results of the comparison of lidar β(9.1) and modeled β(9.1) (Figures 5 and 6).

The ratio β_R = β(9.1)/β(10.6) is shown in Figure 8b, giving a comparison of the lidar β_R [Srivastava et al., 1995] with the β_R obtained from LOPC data. Here, β_R > 2 indicates the presence of an AMS component [Srivastava et al., 1995]. In general, the measured lidar β_R and modeled β_R agreed very well, showing overall similar trends. However, for conditions of rapidly changing air masses (for example, ~0600 UTC on the approach to Tokyo and ~0400 UTC nearer Hawaii), LOPC data do not show the rapid aerosol variation detected by the lidar (as discussed in section 2.2). In low-β conditions 10.6 μm lidar data were close to the detection threshold of ~2 ×10^{-11} m^{-1} sr^{-1}, which made β(10.6) more uncertain, thus adding to lidar β_R variability (for example, around 0300 to 0400 UTC near Darwin and around 0400 to 0500 UTC near Hawaii). Thus, in view of the major differences in the respective instrumentation, sampling, and their limitations, comparison of the two methods, lidar β_R and LOPC modeled β_R, showed reasonably good agreement.

Comparison of the inversion with lidar β_R with volume fractions performed by Srivastava et al. [1995, Figure 4] with that of the volume fraction estimations, V_i' from the LOPC data is shown in Figure 8c. With β at two wavelengths, only two compositions are distinguishable. From 9.1 and 10.6 β_R, AMS can be distinguished (because of its spectral signature at 9.1 μm) from dominant SA in clean conditions or from DS in continental dust, but it is harder to distinguish between SA and DS for intermediate cases. Hence we compared the lidar β_R-inferred AMS volume fraction, V_{AMS}' with the more direct LOPC-estimated V_{AMS}' (from equations (1)-(5) and Figures 5 and 6).

The SA and DS volume fractions combined together can be obtained from V_{SA}' + V_{DS}' =1 - V_{AMS}'. On average, LOPC estimates of V_{AMS}' component showed similar trends to those obtained in lidar-inferred V_{AMS}' in agreement within a factor of 2.

Considering the major differences in the respective instrumentation, sampling, limitations, and uncertainties (see section 2.2) that can contribute to discrepancies in the two data sets, agreement of V_{AMS}' within a factor of 2 is reasonably good. The β_R inversion to V_{AMS}' from the remotely sensed lidar data is subject to the combined two-β uncertainties of ~33% to 52% with possible uncertainties of the simple inversion method used (discussed by Srivastava et al. [1995]). Though the aspirated aerosol size distribution data from LOPC has a lower uncertainty, of ~10% to 20%, it is subject to large particle count (major contribution to the volume) statistics error, which adds more uncertainty to its V_i estimation. Further, there appears to be a general bias in the lidar V_{AMS}', which is lower than LOPC V_{AMS}' by roughly 0.1 to 0.2. This is most likely due to the presence of bisulfates, which were included but not differentiated in LOPC V_{AMS}' from the difference between Ch2 and Ch3, whereas the measured lidar β_R was inverted to V_{AMS}', assuming purely AMS composition and refractive index. (Bisulfate refractive indicies are not well known in infrared, but preliminary absorbance data (S. Johnson, Argonne National Laboratory, private communication, 1991) shows that at 9.1 μm it is lower than AMS, being diluted by the extra acidic component). Bisulfates would tend to lower the effective sulfate (AMS+bisulfate) complex refractive index and would theoretically predict lower β(9.1) and β_R. Thus, to account for the measured β(9.1) to β(10.6) ratio, more AMS+bisulfate component would have to be present (as seen in LOPC data) than if it were pure AMS (as inferred by lidar). So in the measured lidar β_R inversion, if an AMS+bisulfate mixture were to be considered, then inferred V_{AMS}' would come out higher than the pure AMS case. Thus, under the circumstances with lidar and LOPC differences and the additional unaccountability of bisulfates, β_R and V_{AMS}' comparisons do provide the best possible validation for the remote sensing, high-resolution, dual-wavelength lidar β_R ratio technique. Multiple-wavelength lidar observations, set at other component-sensitive wavelengths, would allow further differentiation of SA, DS, and bisulfates.

6. Conclusions

Depending on the atmospheric conditions, aerosol distribution and composition vary dramatically, affecting the scattering properties of aerosols. Since the scattering properties of atmospheric aerosols, which have a major impact on the Earth's climate [Charlson et al., 1991], can vary significantly, it is important to characterize them on a large scale [Penner et al., 1994]. The GLOBE flight mission provided large-scale sampling of aerosol microphysical, chemical, and backscattering properties simultaneously, under a wide range of atmospheric conditions.

Component fractions inferred from the LOPC were used in three different mixture models: externally mixed (EM), mixed-phase sulfate (MPS), and internally mixed composite (IMC). The main conclusion of this paper is that all three models give fairly good agreement with the lidar β and provide a well-defined envelope of the modeling uncertainty itself. However, within this envelope under given atmospheric conditions that govern the complexity of the aerosols, one model sometimes overlaps with lidar data more than the others. The relative
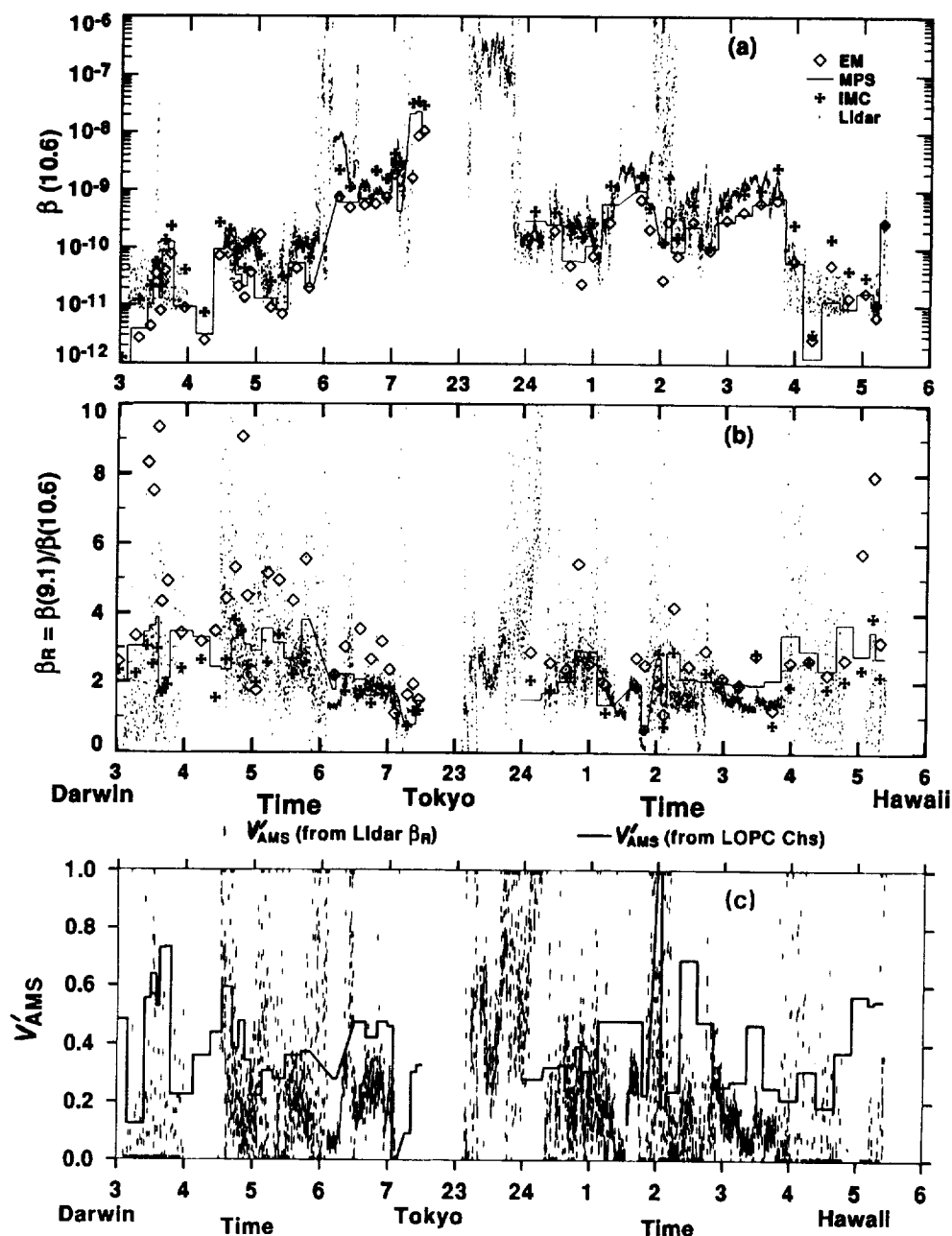
Figure 8. Time series of (a) $\beta(10.6)$ combined for F12 and F14, showing comparison of CW lidar data with EM, MPS, and IMC models, (b) ratio $\beta_R = \beta(9.1)/\beta(10.6)$ from the lidar data in comparison with EM, MPS, and IMC model, and (c) the inferred volume fraction of AMS component, V'_{AMS} from the lidar β_R data as compared with the LOPC data using equations (1)-(5) and integrating over all size bins.

choice of a model is suggested from modeled β values that are most consistent with the lidar β by a comparison of several data points in an air mass or a distinct meteorological feature. The three models chosen for varying complexity of an aerosol system do seem to follow the complexity of the aerosols. The simple EM model is close to lidar data mostly for fresh undisturbed aerosols. However, in general, there is more likelihood of partial mixing of the more reactive aerosol components such as SA and AMS, chemically leading to some bisulfates whose volume fractions, and chemical and optical properties are difficult to quantify. Using physically mixed SA and AMS in an MPS model gave the best overlap with the lidar data for

clean mid-tropospheric aerosol systems. For more well-mixed aged continental-type aerosols in higher loading conditions, such as continental dust plumes and pollution layers, the IMC model gave excellent agreement with the lidar data. The background aerosol feature exhibited both by lidar and by modeled β was best characterized by the MPS model. This also indicated that possible composition of background aerosol may be partially ammoniated SA containing trace amounts of DS. Thus the two lidar and LOPC data sets, keeping in view their individual caveats, complement each other well, giving a more comprehensive picture of the complex atmospheric aerosol system.

References

Baker, W. E., et al., Lidar measured winds from space: An essential component for weather and climate prediction, *Bull. Am. Meteorol. Soc.*, 76, 869-888, 1995.

Bowdle, D. A., J. Rothermel, J. E. Arnold, and S. F. Williams, The Global Backscatter Experiment (GLOBE) Pacific survey mission: Results and implications for LAWS, in *Coherent Laser Radar: Technology and Applications*, OSA Tech. Dig. Ser., 12, 290-292, 1991.

Charlson, R. J., J. Langner, H. Rodhe, C. B. Levoy, and S. G. Warren, Perturbation of the northern hemisphere radiative balance by backscattering from anthropogenic sulfate aerosols, *Tellus, Sec. AB*, 43, 152-163, 1991.

Clarke, A. D., A thermo-optic technique for in-situ analysis of size-resolved aerosol physicochemistry, *Atmos. Environ., Part A*, 25, 635-644, 1991.

Clarke, A. D., Atmospheric nuclei in the Pacific midtroposphere: Their nature, concentration, and evolution, *J. Geophys. Res.*, 98, 20,633-20,647, 1993.

Clarke, A. D., and J. N. Porter, Aerosol size distribution composition and CO_2 backscatter at Mauna Loa Observatory, *J. Geophys. Res.*, 96, 5237-5247, 1991.

Cutten, D. R., R. F. Pueschel, V. Srivastava, D. A. Bowdle, A. D. Clarke, J. Rothermel, R. T. Menzies, and J. D. Spinhirne, Multiwavelength comparison of modeled and measured remote tropospheric aerosol backscatter over Pacific Ocean, *J. Geophys. Res., 101*, 9357-9389, 1996.

Hale, G. M., and M. R. Querry, Optical constants of water in the 200-nm to 200-μm wavelength region, *Appl. Opt.*, 12, 555-563, 1973.

Hanel, G., Properties of atmospheric aerosols as functions of relative humidity at thermodynamic equilibrium with surrounding moist air, *Adv. Geophys.*, 19, 73-188, 1976.

Hanel, G., and M. Lehmann, Equilibrium size of aerosol particles and relative humidity: New experimental data from various aerosol types and their treatment for cloud physics application, *Atmos. Phys.*, 54, 57-71, 1981.

Jarzembski, M. A., V. Srivastava, and D. M. Chambers, Lidar calibration technique using laboratory-generated aerosols, *Appl. Opt.*, 35, 2096-2108, 1996.

Kent, G. S., G. K. Yue, U. O. Farrukh, and A. Deepak, Modelling atmospheric aerosol backscatter at CO_2 wavelengths, 1, Aerosol properties, modeling techniques, and associated problems, *Appl. Opt.*, 22, 1655-1665, 1983.

Kent, G. S., P.-H. Wang, M. P. McCormick, and K. M. Skeens, Multiyear Stratospheric Aerosol and Gas Experiment II measurements of upper troposphere aerosol characteristics, *J. Geophys. Res.*, 100, 13,875-13,899, 1995.

Mie, G., A contribution to the optics of turbid media, especially colloidal metallic suspensions, *Ann. Phys.*, 25, 377-445, 1908.

Menzies, R. T., and D. M. Tratt, Airborne CO_2 coherent lidar for measurements of atmospheric aerosol and cloud backscatter, *Appl. Opt.*, 24, 5698-5711, 1994.

Palmer, K. F., and D. Williams, Optical constants of sulfuric acid: Application to Venus, *Appl. Opt.*, 14, 208-219, 1976.

Penner, J. E., R. J. Charlson, J. M. Hales, N. Laulainen, R. Leifer, T. Novakov, J. Ogren, L. F. Radke, S. E. Schwartz, and L. Travis, Quantifying and minimizing uncertainty of climate forcing by anthropogenic aerosols, *Bull. Am. Meteorol. Soc.*, 75, 375-400, 1994.

Porter, J. A., A. D. Clarke, and R. F. Pueschel, Aircraft studies of size-dependent aerosol sampling through inlets, *J. Geophys. Res.*, 97, 3815-3824, 1992.

Post, M. J., Aerosol backscattering profiles at CO_2 wavelengths: The NOAA data base, *Appl. Opt.*, 23, 2507-2509, 1984.

Prospero, J. M., R. J. Charlson, V. Mohnen, R. Jaenicke, A. C. Delany, J. Moyers, W. Zoller, and K. Rahn, The atmospheric aerosol system: An overview, *Rev. Geophys.*, 21, 1607-1629, 1983.

Pueschel, R. F., J. M. Livingston, G. V. Ferry, and T. E. DeFelice, Aerosol abundances and optical characteristics in the Pacific basin free troposphere, *Atmos. Environ.*, 28, 951-960, 1994.

Rothermel, J., D. A. Bowdle, J. M. Vaughan, and M. J. Post, Evidence of a tropospheric aerosol background backscatter mode, *Appl. Opt.*, 28, 1040-1042, 1989.

Rothermel, J., D. A. Bowdle, and V. Srivastava, Mid-tropospheric aerosol backscatter background mode over the Pacific Ocean at 9.1 μm wavelength, *Geophys. Res. Lett.*, 23, 281-284, 1996a.

Rothermel J., D. M. Chambers, M. A. Jarzembski, V. Srivastava, D. A. Bowdle, and W. D. Jones, Signal processing and calibration of continuous-wave focused CO_2 Doppler lidars for atmospheric backscatter measurement, *Appl. Opt.*, 35, 2083-2095, 1996b.

Shettle, E. R., and R. W. Fenn, Models for aerosols of lower atmosphere and the effects of humidity variations on their optical properties, *Rep. AFGL-TR-79-0214*, pp. 17-18, Air Force Geophys. Lab., Hansom Air Force Base, Bedford, Mass., 1979.

Srivastava, V., Light scattering by inhomogeneous composite particles, Ph.D. dissertation, State Univ. of New York, Albany, 1988.

Srivastava, V., M. A. Jarzembski, and D. A. Bowdle, Comparison of calculated aerosol backscatter at 9.1 and 2.1 wavelengths, *Appl. Opt.*, 31, 1904-1906, 1992.

Srivastava, V., D. A. Bowdle, M. A. Jarzembski, J. Rothermel, D. M. Chambers, and D. R. Cutten, High-resolution remote sensing of atmospheric sulfate aerosols from backscatter using focused CO_2 Doppler lidars, *Geophys. Res. Lett.*, 22, 2373-2376, 1995.

Tang, I. N., and H. R. Munkelwitz, Aerosol growth studies, III, Ammonium bisulfate aerosols in a moist atmosphere, *J. Aerosol Sci.*, 8, 321-330, 1977.

Tang, I. N., H. R. Munkelwitz, and J. G. Davis, Aerosol growth studies, IV, Phase transformations of mixed salt aerosols in a moist atmosphere, *J. Aerosol Sci.*, 9, 505-511, 1978.

Toon, O. B., J. B. Pollack, and B. N. Khare, Optical constants of several atmospheric species: Ammonium sulfate, aluminum oxide, and sodium chloride, *J. Geophys. Res.*, 81, 5733-5748, 1976.

Tratt, D. M., and R. T. Menzies, Recent climatological trends in atmospheric aerosol backscatter derived from the Jet Propulsion Laboratory multiyear backscatter profile database, *Appl. Opt.*, 33, 424-430, 1994.

Vaughan, J. M., R. D. Callan, D. A. Bowdle, and J. Rothermel, Spectral analysis, digital integration and measurement of low backscatter in coherent laser radar, *Appl. Opt.*, 28, 3008-3014, 1989.

Vaughan, J. M., D. W. Brown, C. Nash, S. B. Alejandro, and G. G. Koenig, Atlantic atmospheric aerosol studies, 2, Compendium of airborne backscatter measurements at 10.6 μm, *J. Geophys. Res.*, 100, 1043-1065, 1995.

Willeke, K., and P. A. Baron (Eds.), *Aerosol Measurements: Principles, Techniques, and Applications*, chap. 7, 12, 13, Van Nostrand Reinhold, New York, 1993.

A.D. Clarke, Department of Oceanography, University of Hawaii, Honolulu, HI 96822.

M.A. Jarzembski, J. Rothermel, and V. Srivastava, NASA Global Hydrology and Climate Center, 977 Explorer Boulevard, Huntsville, AL 35805. (e-mail: vandana.srivastava@msfc.nasa.gov)